

Article

# Enhanced Photodegradation of Synthetic Dyes Mediated by $\text{Ag}_3\text{PO}_4$ -Based Semiconductors under Visible Light Irradiation

Alice Pavanello, Alejandro Blasco, Peter F. Johnston, Miguel A. Miranda \*   
and Maria Luisa Marin \* 

Instituto de Tecnología Química, Universitat Politècnica de València-Consejo Superior de Investigaciones Científicas, Avda. de los Naranjos s/n, E-46022 Valencia, Spain; alpa13a@itq.upv.es (A.P.); alblabru@upvnet.upv.es (A.B.); peterjohnston@outlook.com (P.F.J.)

\* Correspondence: mmiranda@qim.upv.es (M.A.M.); marmarin@qim.upv.es (M.L.M.);  
Tel.: +34-963877807 (M.A.M.); +34-963877815 (M.L.M.)

Received: 30 May 2020; Accepted: 9 July 2020; Published: 11 July 2020



**Abstract:** Four silver phosphate-based materials were successfully synthesized, characterized, and evaluated, together with  $\text{TiO}_2$ , in the photodegradation of synthetic dyes (tartrazine, Orange II, rhodamine, and Brilliant Blue FCF) under two irradiation sources centered at 420 and 450 nm. Scanning Electron Microscopy (SEM) images showed different topologies of the synthesized materials, whereas diffuse reflectance spectra demonstrated that they display absorption up to 500 nm. Degradation experiments were performed in parallel with the silver materials and  $\text{TiO}_2$ . Upon irradiation centered at 420 nm, the abatement of the dyes was slightly more efficient in the case of  $\text{TiO}_2$ —except for Orange II. Nevertheless, upon irradiation centered at 450 nm,  $\text{TiO}_2$  demonstrated complete inefficiency and silver phosphates accomplished the complete abatement of the dyes—except for Brilliant Blue FCF. A careful analysis of the achieved degradation of dyes revealed that the main reaction mechanism involves electron transfer to the photogenerated holes in the valence band of silver photocatalysts, together with the direct excitation of dyes and the subsequent formation of reactive species. The performance of  $\text{TiO}_2$  was only comparable at the shorter wavelength when hydroxyl radicals could be formed; however, it could not compete under irradiation at 450 nm since the formed superoxide anion is not as reactive as hydroxyl radicals.

**Keywords:** conduction band; hole; hydroxyl radical; mechanism; superoxide anion; titanium dioxide; valence band

## 1. Introduction

The availability of drinking water of good quality is essential to human development. However, there is a stress on natural water resources associated with the increasing population trend that could be mitigated by adopting more sustainable policies to minimize water pollution, such as managing waste effectively. In parallel, more efficient treatments for wastewater are still desirable and constitute a current demand [1–4]. Synthetic dyes are among the contaminants that are recalcitrant to conventional wastewater treatments [5], and although most of them are not intrinsically toxic, they pose problems to water-based ecosystems because they remain fairly stable under visible light, acting as light filters that would otherwise be used by algae and other aquatic plants [6]. Moreover, they exhibit a huge variety of chemical structures that make their degradation challenging [7].

Advanced oxidation processes such as photo-Fenton and the use of the heterogeneous semiconductor  $\text{TiO}_2$  are among the photocatalytic approaches that have been tested to produce the abatement of these contaminants [8,9]. In both cases, under solar light irradiation, the highly oxidizing

hydroxyl radical is produced, which subsequently degrades most organic compounds, regardless of their chemical structure [10]. However, several disadvantages limit the practical applications of TiO<sub>2</sub>. Among them are its large intrinsic band-gap ( $E_g$  of approximately 3.2 eV), which limits the use of solar light to the UV region (only approximately 4% of solar radiation), and the energy waste associated with fast recombination of the photogenerated free  $e^-$  in the conduction band (CB) and the hole ( $h^+$ ) in the valence band (VB) [11]. Thus, different attempts have been made to enlarge the capability of TiO<sub>2</sub> to absorb visible light, such as preparing hybrids with other metals [8,12–15]. Moreover, the synthesis and use of other semiconductors has also been reviewed [16–18].

On the other hand, the potential of a semiconductor to produce a hydroxyl radical from the  $h^+$  photogenerated in the VB depends, among other things, on the potential value. When such a value is below the redox potential of the hydroxyl radical ( $E^\circ \text{ OH}/\text{H}_2\text{O} = +2.27 \text{ V vs. normal hydrogen electrode (NHE)}$ ) [9], the generation of this intermediate is not thermodynamically feasible; however,  $h^+$  (VB) could be oxidizing enough to produce the abatement of the pollutants through direct electron transfer.

Moreover, if the semiconductor is able to absorb visible light, it could be even more efficient than TiO<sub>2</sub> at producing the solar photodegradation of dyes in wastewaters. In this sense, the recently synthesized Ag<sub>3</sub>PO<sub>4</sub> appears to be a suitable alternative, since it can absorb solar light of wavelengths shorter than 530 nm as a result of its indirect band-gap of 2.36 eV and direct transition of 2.45 eV [19,20]. Interestingly, its highly dispersive conduction and valence bands result in an unlikely recombination of electron-hole pairs. The band edge potential values determined for the CB and VB of Ag<sub>3</sub>PO<sub>4</sub> are 0.45 and 2.9 eV, respectively [19,21]. Thus, the formation of OH· radicals from the holes photogenerated in its VB is thermodynamically feasible, whereas the formation of superoxide anions is thermodynamically disfavored because  $E^\circ (\text{O}_2/\text{O}_2^{\cdot-}) = -0.33 \text{ V vs. NHE}$  [22] is more negative than the CB of Ag<sub>3</sub>PO<sub>4</sub>. Furthermore, the CB  $e^-$  of Ag<sub>3</sub>PO<sub>4</sub> could reduce O<sub>2</sub> to H<sub>2</sub>O<sub>2</sub> through a two-electron reduction  $E^\circ (\text{O}_2/\text{H}_2\text{O}_2) = +0.87 \text{ V vs. NHE}$  [22]. Nonetheless, being thermodynamically feasible does not guarantee that a reaction will proceed because kinetics also play a crucial role [23].

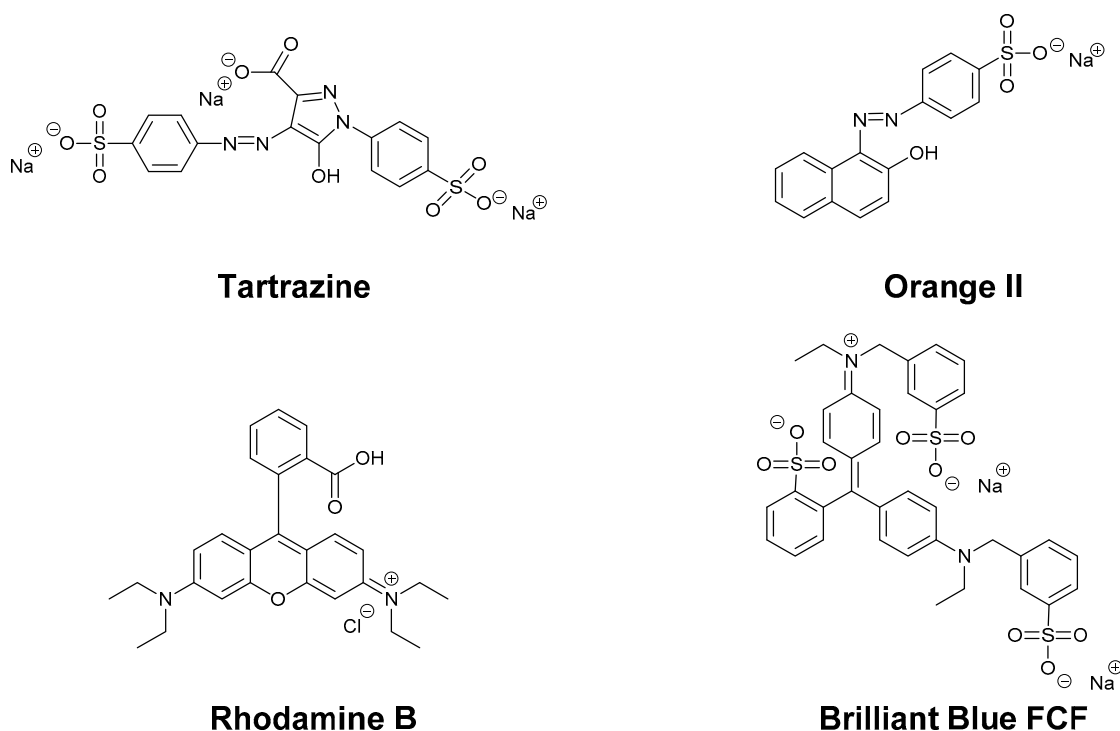
In the literature, controversial results have been reported on the generation of hydroxyl radicals and superoxide radical anions upon the illumination of Ag<sub>3</sub>PO<sub>4</sub> in the photocatalytic degradation of a variety of pollutants [24–35]. Nevertheless, excited Ag<sub>3</sub>PO<sub>4</sub> could still act as an oxidant via  $h^+$  (VB).

Furthermore, new composites such as Ag<sub>3</sub>PO<sub>4</sub>/TiO<sub>2</sub> (3/97, wt.% ratio) have been demonstrated to be efficient in the photodegradation of *p*-nitrophenol [36] and in the decomposition of isopropanol by visible light photosensitization of Ag<sub>3</sub>PO<sub>4</sub>, probably as a result of the hole transfer from Ag<sub>3</sub>PO<sub>4</sub> to TiO<sub>2</sub> and subsequent hydroxyl radical generation, although a rigorous study to evaluate the contribution of the different reactive species to the degradation of isopropanol has not been performed [37].

With this background, in the present paper, we intended to compare the performance of OH· vs.  $h^+$  (VB) in the photodegradation of a variety of synthetic dyes. With this purpose, we prepared Ag<sub>3</sub>PO<sub>4</sub> with different morphologies and used them together with commercial TiO<sub>2</sub> and a hybrid Ag<sub>3</sub>PO<sub>4</sub>-TiO<sub>2</sub> to compare their efficiency in the photodegradation of a variety of dyes using artificial light. The selection of dyes included tartrazine, Orange II [38], rhodamine B [39] and Brilliant Blue FCF (Table 1; Figure 1 and Figure S1). Tartrazine and Orange II constitute two examples of azo dyes that have been mainly used as color additives in food and beverages; rhodamine B is a synthetic xanthene-like dye with wide applications in biology as a tracer, and Brilliant Blue FCF belongs to the family of triphenylmethane dyes and is commonly used to color beverages, dairy products, powders, and syrups.

**Table 1.** Photophysical properties and electrochemical data of the selected synthetic dyes [40]. NHE: normal hydrogen electrode.

Dye	Max (nm)	(M <sup>-1</sup> cm <sup>-1</sup> )	E <sub>ox</sub> (dye <sup>+</sup> /dye, V vs. NHE)	E (HOMO–LUMO Gap, eV)	E <sub>ox</sub> <sup>*</sup> (dye <sup>+</sup> / <sup>+</sup> dye <sup>*</sup> , V vs. NHE)
Tartrazine (TZ)	429.5 [41]	20,810 [41]	+1.25 [42]	2.33	−1.08 [41]
Orange II (OII)	480 [43]	15,400 [43]	+0.76 [44]	2.36 [45]	−1.60 [45]
Rhodamine B (RhB)	545 [43]	106,000 [43]	+1.15 [46]	2.22 [46]	−1.07 [46]
Brilliant Blue FCF (BB)	625 [47]	97,000 [47]	+1.06 [42]	1.86	−0.80

**Figure 1.** Chemical structures of the selected synthetic dyes.

## 2. Results and Discussion

### 2.1. Characterization

Four different photocatalysts were prepared following slight modifications of previously reported protocols. The morphology of the synthesized materials was determined by means of SEM (Figure 2). Figure 2a shows cubic Ag<sub>3</sub>PO<sub>4</sub> in a variation in magnification (2600×, top left, to 28,200×, bottom right). Regular cubes are seen, and these have equidistant edges and flat faces with an average diameter of 1360 nm [20]. Figure 2b shows the rhombic dodecahedron Ag<sub>3</sub>PO<sub>4</sub> in a range of magnifications (6000×, top left, to 34,700×, bottom right). Though irregular, a common rhombic dodecahedron shape can be seen throughout, which accords with previously reported composites. The images show a smaller average diameter than those previously described (a mean diameter of 340 nm vs. reported 600 nm) and a higher polydispersity [20]. Figure 2c illustrates synthesized spherical Ag<sub>3</sub>PO<sub>4</sub> catalysts with irregular sizes in a variation in magnification from 11,300× (top left) to 90,400× (bottom right). Finally, Figure 2d shows the hybrid Ag<sub>3</sub>PO<sub>4</sub>–TiO<sub>2</sub> catalyst in a variation in magnification from 3600× (top right) to 56,700× (top left). The bottom image illustrates large Ag<sub>3</sub>PO<sub>4</sub> particles with flat surfaces and smaller TiO<sub>2</sub> particles deposited on the surface [48].

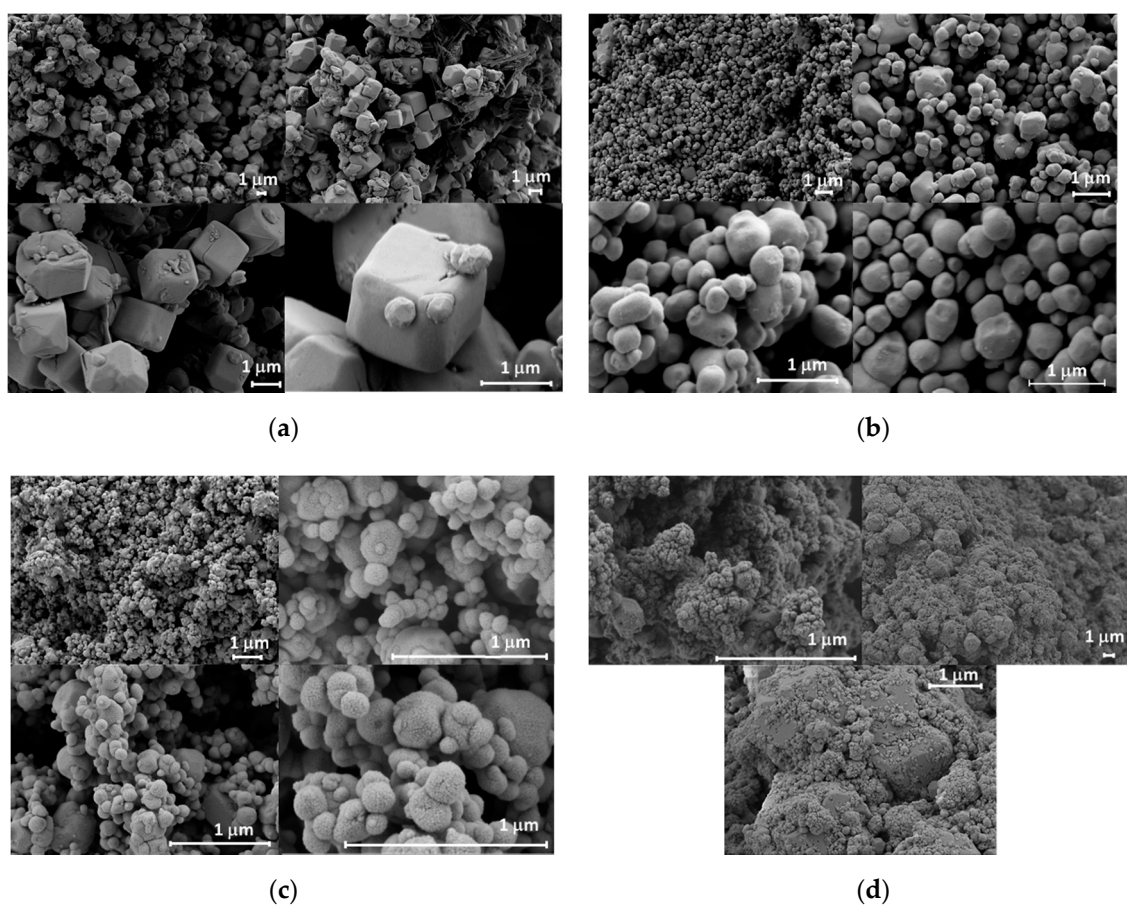


**Figure 2.** SEM Images of the synthesized photocatalysts: (a) Cubic  $\text{Ag}_3\text{PO}_4$ , (b) rhombic dodecahedron  $\text{Ag}_3\text{PO}_4$ , (c) spherical  $\text{Ag}_3\text{PO}_4$ , and (d) hybrid  $\text{Ag}_3\text{PO}_4\text{-TiO}_2$ .

The potential of the synthesized catalysts to act as visible-light photocatalysts was initially investigated by recording their diffuse reflectance spectra. The absorbance ( $F(R)$ ) was obtained by a transformation based on the Kubelka–Munk function (Figure 3a). All  $\text{Ag}_3\text{PO}_4$  photocatalysts significantly absorbed in the visible region, with the rhombic dodecahedrons, spheres, and hybrid heterostructures absorbing up to 500 nm and the cubes extending the absorption by up to 525 nm. They showed a clear improvement in the absorbance of the solar spectrum when compared to  $\text{TiO}_2$ , which has a measured upper absorbance limit of 385 nm. The band-gap values were determined from the intercepts of the Tauc plots obtained by plotting  $(F(R) * h)^{1/2}$  versus photon energy ( $h$ ) in eV (Figure 3b). The determined indirect band-gap values of  $\text{Ag}_3\text{PO}_4$  were slightly dependent on the morphologies: 2.32, 2.35, and 2.26 eV for the cubes, rhombic dodecahedrons, and spheres, respectively. The hybrid  $\text{Ag}_3\text{PO}_4\text{-TiO}_2$  catalyst gave two values: 3.09 and 2.28 eV, in agreement with the present two substances; finally, the determined band-gap value for the commercial  $\text{TiO}_2$  was 3.23 eV. All the experimental values were similar to those reported in the literature for analogous materials [9,19,37].

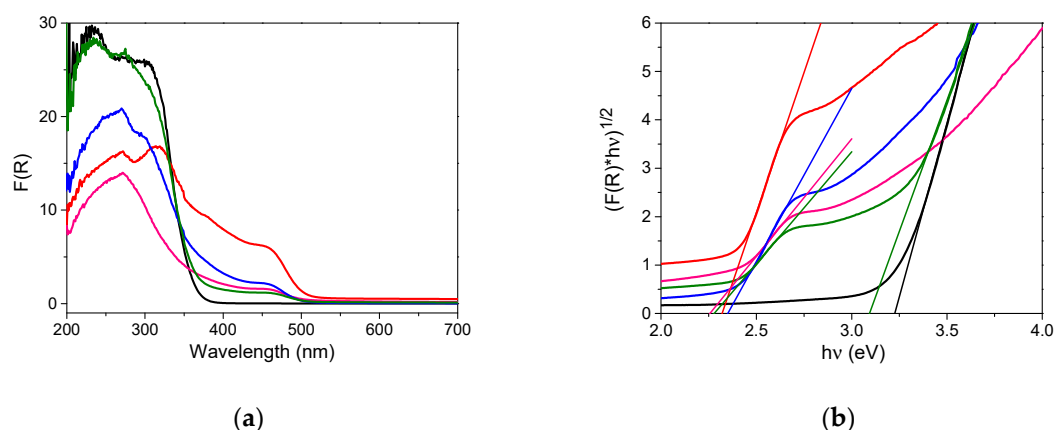


**Figure 3.** Kubelka–Munk diffusion reflectance UV–visible spectra (a) and Tauc plots for indirect band-gap determination (b) of the synthesized  $\text{Ag}_3\text{PO}_4$ -based catalysts and the commercial  $\text{TiO}_2$ : cubes (red), rhombic dodecahedrons (blue), spheres (pink), hybrid  $\text{Ag}_3\text{PO}_4\text{-TiO}_2$  (green), and  $\text{TiO}_2$  (black). Linear fittings to estimate the band-gaps are shown.

## 2.2. Photocatalytic Activity

The photocatalytic performance of the different photocatalysts was evaluated by assessing the degradation of the selected synthetic dyes under artificial irradiation. To compare the efficiency of the  $h^+$  vs. the  $\text{OH}\cdot$  or the injection of an  $e^-$  from the excited states of the dyes into the CB of the photocatalysts, two different irradiation sources were tested: (i) fluorescent lamps with emission centered at 420 nm where all the semiconductors and the azo dyes absorbed and (ii) LEDs centered at 450 nm where only  $\text{Ag}_3\text{PO}_4$ ,  $\text{Ag}_3\text{PO}_4\text{-TiO}_2$  and the azo dyes absorbed, although a small contribution of rhodamine B (RhB) and Brilliant Blue FCF (BB) in the absorption cannot be disregarded. The irradiation times were fixed to ensure that bleaching was not competitive, and controls in the dark were also performed (see Figures S4–S6).

Figure 4 shows the photodegradations achieved upon irradiation centered at 420 nm, and Table 2 contains the pseudo-first order rate constants determined for all the combinations of dye/photocatalyst (see Figure S8 for the linear fittings to a pseudo-first order model). A degradation percentage higher than 90% was achieved in the case of tartrazine (TZ), regardless of the photocatalyst used. The  $\text{Ag}_3\text{PO}_4$  cubes showed less efficiency than other  $\text{Ag}_3\text{PO}_4$  materials, while  $\text{TiO}_2$  appeared to be slightly more successful than the rest of the  $\text{Ag}_3\text{PO}_4$  catalysts. In the case of Orange II (OII), the observed photodegradation followed a completely different trend, as in this case,  $\text{Ag}_3\text{PO}_4$  photocatalysts were much more efficient than  $\text{TiO}_2$ . Finally, in the case of RhB and BB, their photodegradations in the presence of  $\text{Ag}_3\text{PO}_4$  were generally much slower than those observed for TZ and OII, while when  $\text{TiO}_2$  was used, similar values to those found for the azo dyes were determined. Thus, the filter action of the dyes did not appear to have an influence on the performance of  $\text{TiO}_2$ , regardless of the absorbance at 420 nm for OII being approximately one third of that of TZ or the fact that RhB and BB could not absorb/filter light at 420 nm (Table 1 and Figure S1). Analogously, the potential contribution of the direct excitation of the dyes followed by the injection of an  $e^-$  into the CB of  $\text{TiO}_2$  looked negligible; thus, results pointed to the hydroxyl radical as the oxidant responsible for the degradation of the studied dyes in the photodegradations catalyzed by  $\text{TiO}_2$  [44,49]. On the contrary, in the case of the  $\text{Ag}_3\text{PO}_4$  materials, the values of the pseudo-first order rate constants for the photodegradations of these dyes could be related to their chemical structure, as RhB and BB are more reluctant to oxidation than the TZ and OII azo dyes.

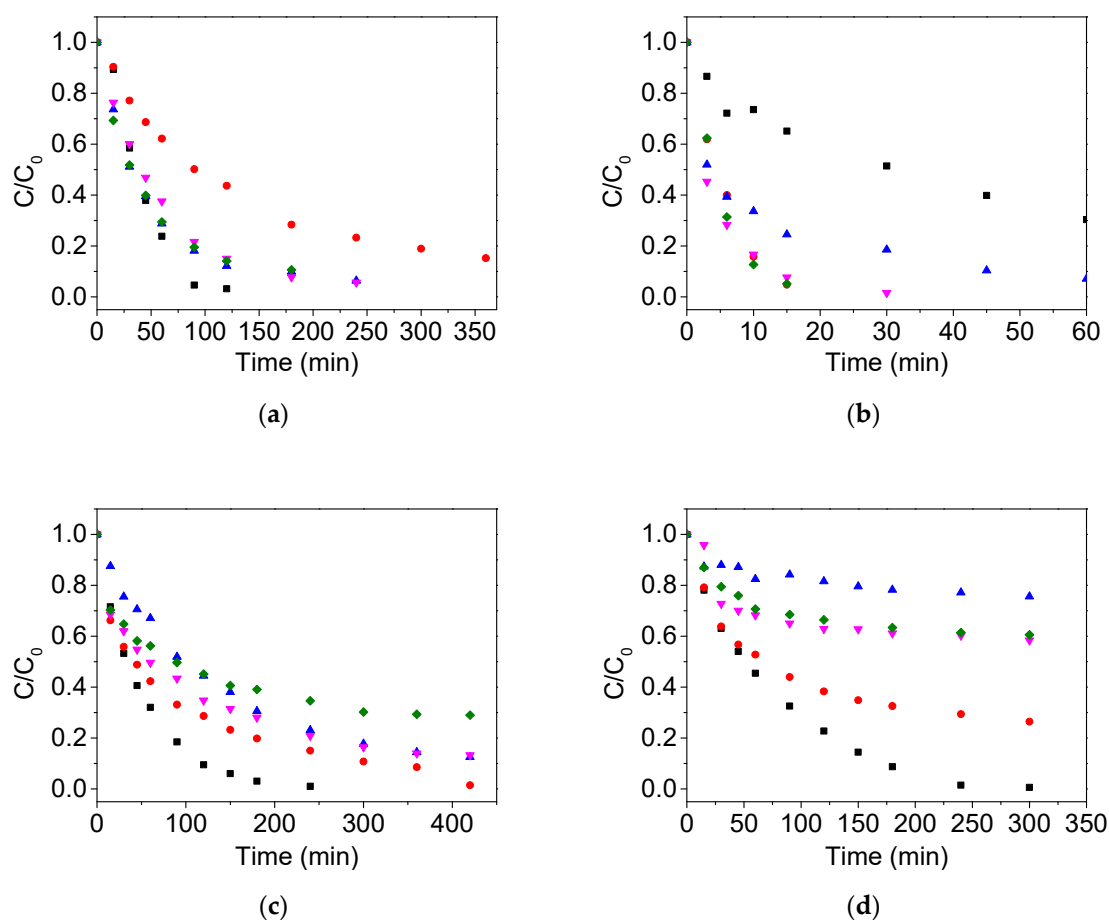


**Figure 4.** Relative concentration of tartrazine (TZ) (a), Orange II (OII) (b), rhodamine blue (RhB) (c), and Brilliant Blue FCF (BB) (d) vs. time in the presence of  $\text{Ag}_3\text{PO}_4$  cubes ( $\bullet$ ),  $\text{Ag}_3\text{PO}_4$  rhombic dodecahedrons ( $\blacktriangle$ ),  $\text{Ag}_3\text{PO}_4$  spheres ( $\blacktriangledown$ ), hybrid  $\text{Ag}_3\text{PO}_4\text{-TiO}_2$  ( $\blacklozenge$ ), or  $\text{TiO}_2$  ( $\blacksquare$ ) under 420 nm irradiation. Initial concentrations:  $5 \times 10^{-5}$  M (dye) and 0.5 g/L (photocatalyst) in aerated aqueous media.

**Table 2.** Pseudo-first order constants ( $\text{min}^{-1}$ ) determined for the photodegradations performed under 420 nm irradiation.

Photocatalyst	TZ	OII	RhB	BB
$\text{Ag}_3\text{PO}_4$ cubes	$6.9 \times 10^{-3}$	$2.0 \times 10^{-1}$	$8.1 \times 10^{-3}$	$8.8 \times 10^{-3}$
$\text{Ag}_3\text{PO}_4$ rhombic dodecahedrons	$1.8 \times 10^{-3}$	$8.5 \times 10^{-2}$	$6.1 \times 10^{-3}$	$5.4 \times 10^{-4}$
$\text{Ag}_3\text{PO}_4$ spheres	$1.6 \times 10^{-2}$	$1.3 \times 10^{-1}$	$5.4 \times 10^{-3}$	$5.1 \times 10^{-3}$
$\text{TiO}_2\text{-Ag}_3\text{PO}_4$	$1.8 \times 10^{-2}$	$2.0 \times 10^{-1}$	$4.4 \times 10^{-3}$	$4.0 \times 10^{-3}$
$\text{TiO}_2$	$1.9 \times 10^{-2}$	$1.8 \times 10^{-2}$	$1.9 \times 10^{-2}$	$1.3 \times 10^{-2}$

Figure 5 shows the photodegradations achieved upon irradiation centered at 450 nm, and Table 3 contains the pseudo-first order rate constants determined for all the combinations of dye/photocatalyst (see Figure S9 for the linear fittings to a pseudo-first order model). The abatement of the two azo dyes, TZ and OII, catalyzed by the silver materials was very efficient, while  $\text{TiO}_2$  demonstrated a complete inefficiency at this wavelength for those pollutants. For the case of RhB,  $\text{TiO}_2$  was only able to produce the abatement of RhB in a 40% yield, while  $\text{Ag}_3\text{PO}_4$  was very efficient [21,50]. Lastly, the photodegradation of BB at 450 nm only arrived at 60% abatement when the hybrid was used. In fact, the photodegradation of BB was only successful at percentages higher than 90% when  $\text{TiO}_2$  was employed at 420 nm. Overall, the performance of the hybrid material was analogous to the rest of the silver-based ones [51,52]. The injection of an  $e^-$  from the excited RhB into the CB of  $\text{TiO}_2$  appeared

as the more likely photodegradation pathway for the case of RhB, while this was not operating in the case of TZ, OII, or BB.

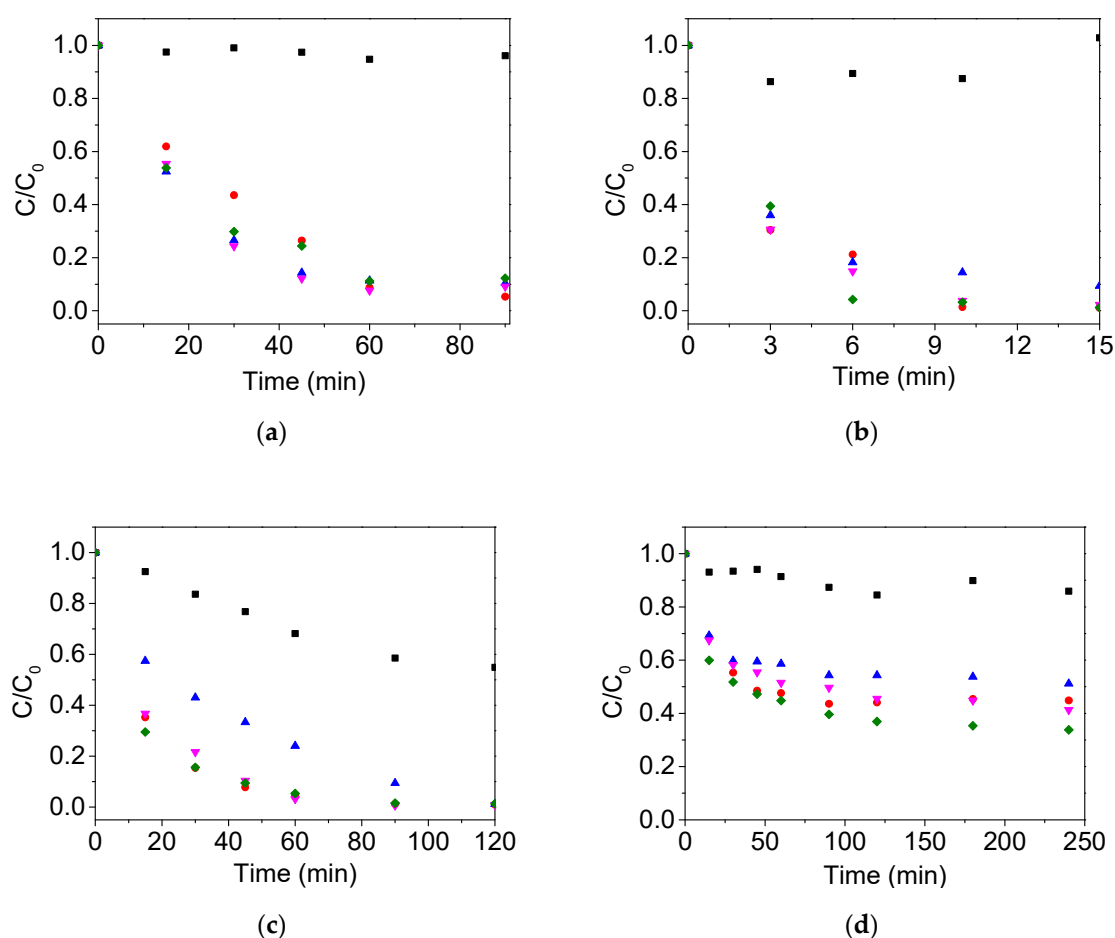


**Figure 5.** Relative concentration of TZ (a), OII (b), RhB (c) and BB (d) vs. time in the presence of  $\text{Ag}_3\text{PO}_4$  cubes (●),  $\text{Ag}_3\text{PO}_4$  rhombic dodecahedrons (▲),  $\text{Ag}_3\text{PO}_4$  spheres (▼), hybrid  $\text{Ag}_3\text{PO}_4\text{-TiO}_2$  (◆), or  $\text{TiO}_2$  (■), under 450 nm irradiation. Initial concentrations:  $5 \times 10^{-5}$  M (dye) and 0.5 g/L (photocatalyst) in aerated aqueous media.

**Table 3.** Pseudo-first order constants ( $\text{min}^{-1}$ ) determined for the photodegradations performed under 450 nm irradiation.

Photocatalyst	TZ	OII	RhB	BB
$\text{Ag}_3\text{PO}_4$ cubes	$3.5 \times 10^{-2}$	$4.1 \times 10^{-1}$	$4.8 \times 10^{-2}$	$1.2 \times 10^{-2}$
$\text{Ag}_3\text{PO}_4$ rhombic dodecahedrons	$4.3 \times 10^{-2}$	$2.8 \times 10^{-1}$	$2.5 \times 10^{-2}$	$1.7 \times 10^{-2}$
$\text{Ag}_3\text{PO}_4$ spheres	$4.4 \times 10^{-2}$	$3.2 \times 10^{-1}$	$5.6 \times 10^{-2}$	$1.0 \times 10^{-2}$
$\text{TiO}_2\text{-Ag}_3\text{PO}_4$	$3.4 \times 10^{-2}$	$3.0 \times 10^{-1}$	$4.4 \times 10^{-2}$	$1.6 \times 10^{-2}$
$\text{TiO}_2$	$5.7 \times 10^{-4}$	$6.7 \times 10^{-4}$	$4.7 \times 10^{-3}$	$8.1 \times 10^{-4}$

### 2.3. Formation of Reactive Oxygen Species

Different reactive species including  $\text{OH}\cdot$ ,  $\text{O}_2\cdot^-$ , and  $\text{h}^+$  can be involved in heterogeneous photocatalytic oxidation processes. To assess their role in the reaction mechanisms, a variety of scavengers can be used. Sometimes, this may be misleading due to the incomplete species selectivity of the scavengers, but it is the method of choice when the direct detection of the reaction intermediates using time-resolved spectroscopy is not possible. Hence, the effect of 2-propanol (IPA), *p*-benzoquinone (BQ), and ammonium oxalate (AO) as scavengers of  $\text{OH}\cdot$ ,  $\text{O}_2\cdot^-$ , and  $\text{h}^+$ , respectively, was investigated

in the photodegradation of TZ, AOII, RhB, and BB in an attempt to elucidate the operating reaction mechanisms [21,53,54]. The obtained results for the irradiations performed at 420 and 450 nm are shown in Figures 6 and 7, respectively. As illustrated in Figure 6a, the photodegradation of TZ was remarkably suppressed by the addition of BQ in all cases, while AO only decreased the efficiency of  $\text{Ag}_3\text{PO}_4$  and  $\text{Ag}_3\text{PO}_4\text{-TiO}_2$ ; finally, the effect of IPA was higher for  $\text{Ag}_3\text{PO}_4\text{-TiO}_2$  than for  $\text{TiO}_2$ . The results obtained for OII (Figure 6b) showed that in the case of  $\text{Ag}_3\text{PO}_4$  and  $\text{Ag}_3\text{PO}_4\text{-TiO}_2$ , the effect of the scavengers was  $\text{BQ} > \text{AO} > \text{IPA}$ , while for  $\text{TiO}_2$ , the order was  $\text{IPA} > \text{BQ} > \text{AO}$ . Interestingly, in the photodegradation of RhB (Figure 6c) by  $\text{Ag}_3\text{PO}_4$ , only AO was effective, while  $\text{BQ}^- \gg \gg \text{AO}$  was observed in the presence of  $\text{Ag}_3\text{PO}_4\text{-TiO}_2$ ; finally,  $\text{BQ} \gg \gg \text{IPA}$  when  $\text{TiO}_2$  was employed. For BB (Figure 6d), the obtained results indicated that the main scavengers were  $\text{BQ} \gg \gg \text{AO}$  or  $\text{IPA}$  for  $\text{Ag}_3\text{PO}_4$  and  $\text{Ag}_3\text{PO}_4\text{-TiO}_2$ , while the order was  $\text{AO} > \text{BQ}$  in the case of  $\text{TiO}_2$ .

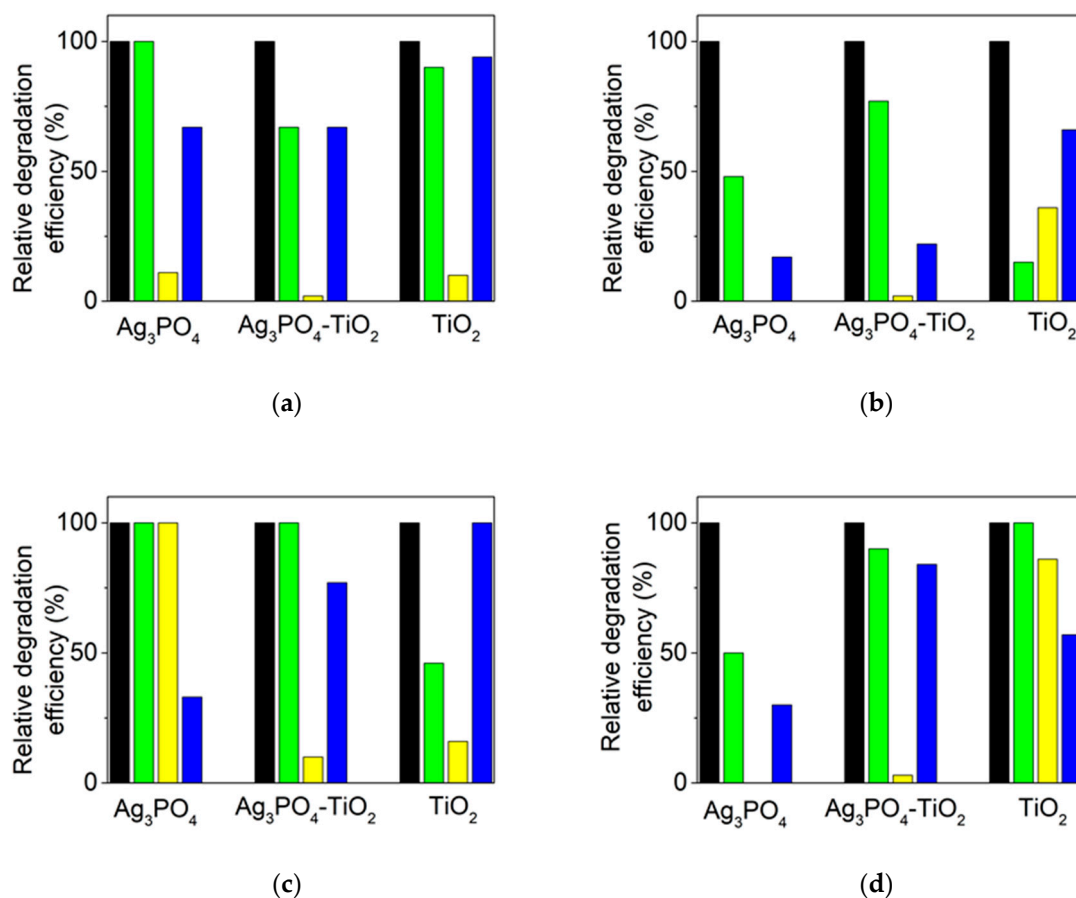


**Figure 6.** Effect of different scavengers on the relative degradation efficiency of TZ (a), OII (b), RhB (c), and BB (d) in the presence of  $\text{Ag}_3\text{PO}_4$ , hybrid  $\text{Ag}_3\text{PO}_4\text{-TiO}_2$ , and  $\text{TiO}_2$ , under 420 nm irradiation. No scavenger is shown in black, 2-propanol ( $1 \times 10^{-1}$  M) is shown in green, *p*-benzoquinone ( $1 \times 10^{-4}$  M) is shown in yellow, and ammonium oxalate ( $1 \times 10^{-4}$  M) is shown in blue. Initial concentrations:  $5 \times 10^{-5}$  M (dye) and 0.5 g/L (photocatalyst) in aerated aqueous media.

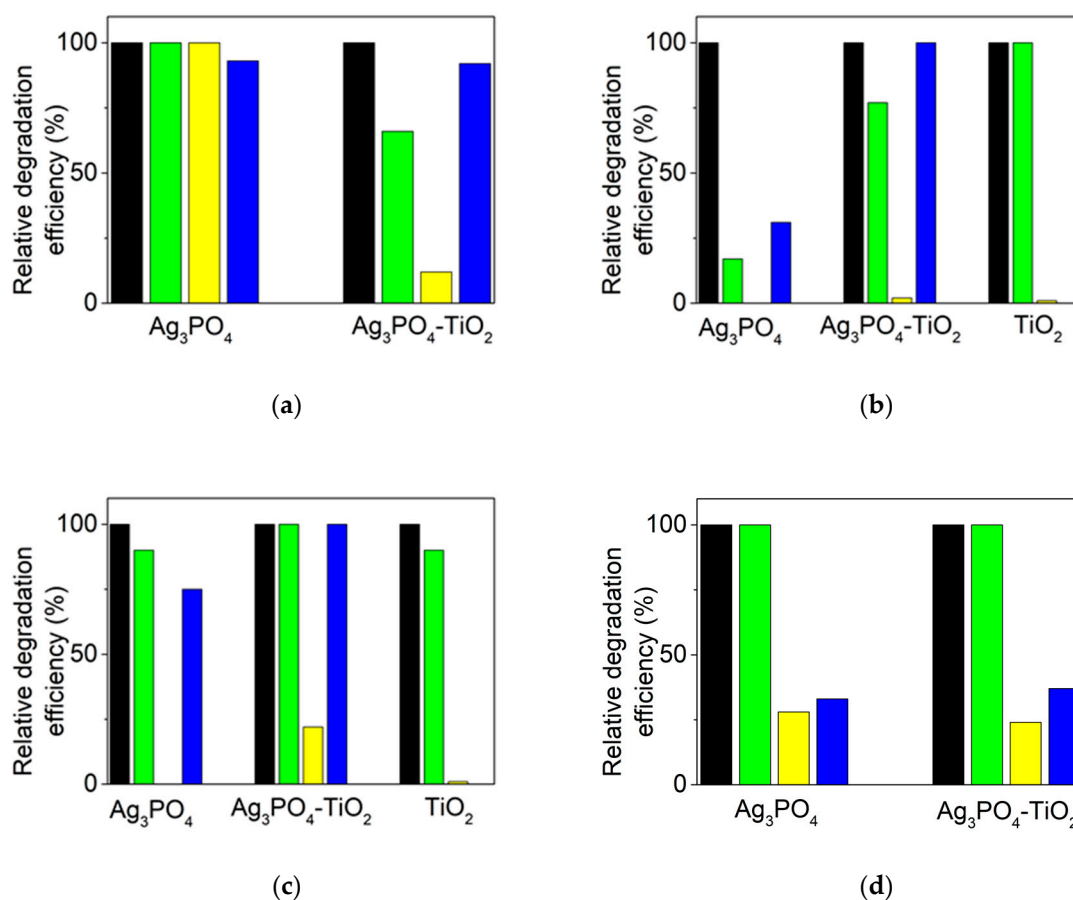


**Figure 7.** Effect of different scavengers on the relative degradation efficiency of TZ (a), OII (b), RhB (c), and BB (d) in the presence of  $\text{Ag}_3\text{PO}_4$ , hybrid  $\text{Ag}_3\text{PO}_4\text{-TiO}_2$ , and  $\text{TiO}_2$ , under 450 nm irradiation. No scavenger is shown in black, 2-propanol ( $1 \times 10^{-1}$  M) is shown in green, *p*-benzoquinone ( $1 \times 10^{-4}$  M) is shown in yellow, and ammonium oxalate ( $1 \times 10^{-4}$  M) is shown in blue. Initial concentrations:  $5 \times 10^{-5}$  M (dye) and 0.5 g/L (photocatalyst) in aerated aqueous media. Note that ammonium oxalate was not employed for  $\text{TiO}_2$ .

The photo-oxidation of TZ at 450 nm (Figure 7a) was mainly inhibited by AO when  $\text{Ag}_3\text{PO}_4$  was employed and by BQ  $\gg$  IPA for  $\text{Ag}_3\text{PO}_4\text{-TiO}_2$ . In the abatement of OII (Figure 7b), the most effective scavenger was BQ in all cases, although marginal effects of IPA for  $\text{Ag}_3\text{PO}_4$  and  $\text{Ag}_3\text{PO}_4\text{-TiO}_2$  cannot be disregarded, as well as AO for  $\text{Ag}_3\text{PO}_4$ . In the case of RhB (Figure 7c), the main scavenger was again BQ for all the photocatalysts. Lastly, the abatement of BB by  $\text{Ag}_3\text{PO}_4$  and  $\text{Ag}_3\text{PO}_4\text{-TiO}_2$  was affected by both BQ and AO.

Furthermore, the formation of  $\text{OH}\cdot$  from the photocatalysts upon illumination was evaluated by fluorescence using terephthalic acid, which is known to react directly with  $\text{OH}\cdot$  to produce 2-hydroxyterephthalic acid, a highly fluorescent product with an emission maximum at 425 nm upon excitation at 315 nm [55,56]. The results are shown in Figure 8a for the  $\text{Ag}_3\text{PO}_4$  cubes, in Figure 8b for  $\text{TiO}_2$ , and in Figure S7 for all the catalysts.

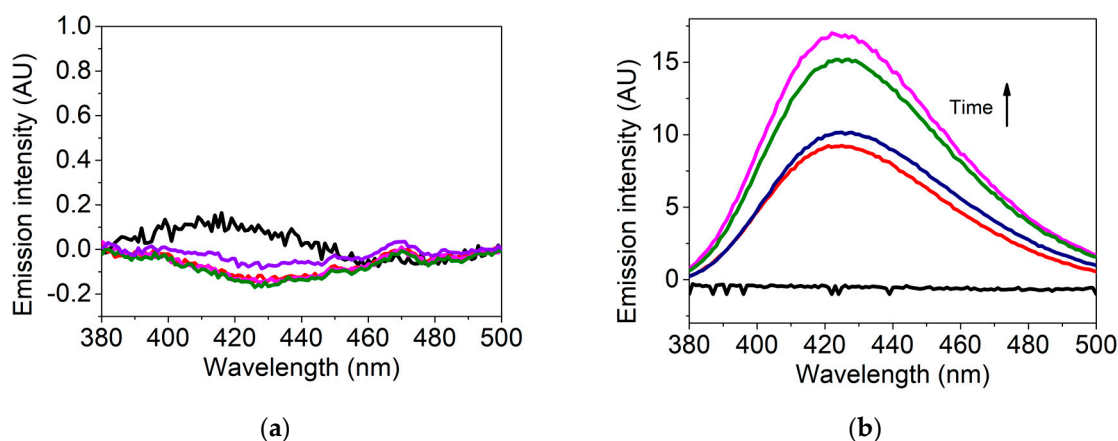
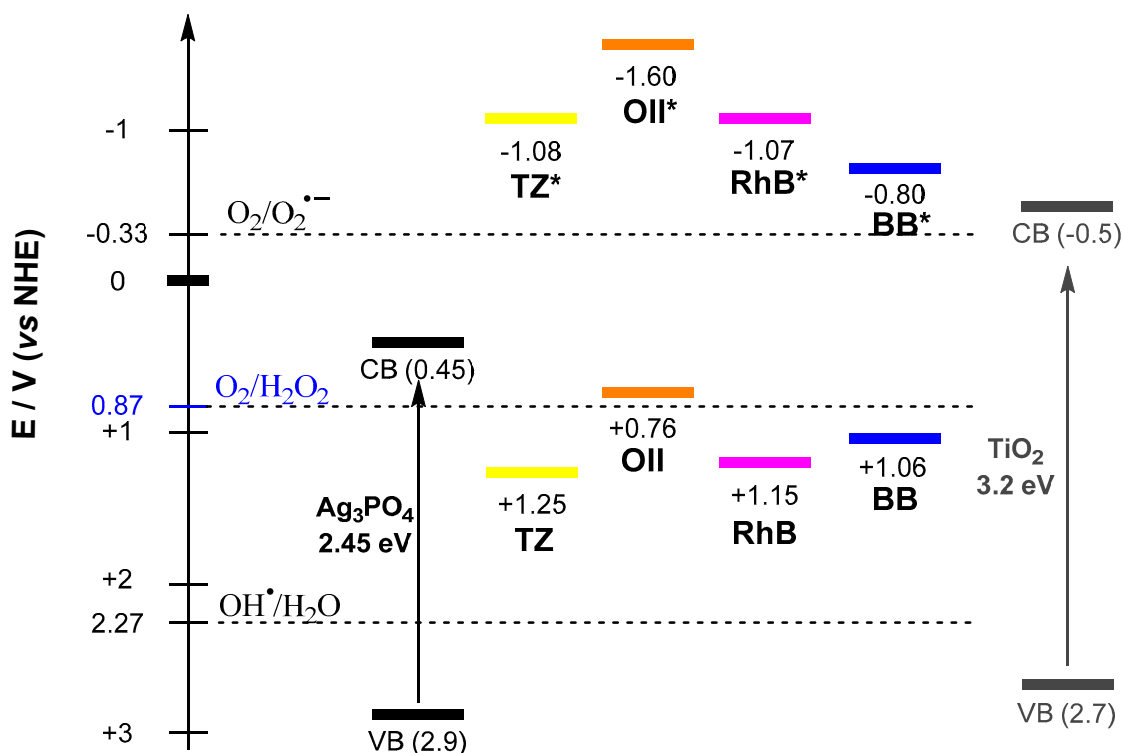


**Figure 8.** Emission spectra of a solution of terephthalic acid (0.5 mM in 2 mM aqueous NaOH) and 0.5 g/L of Ag<sub>3</sub>PO<sub>4</sub> cubes (a) or TiO<sub>2</sub> (b), recorded at different irradiation times: 0 (black), 15 (red), 45 (blue), 60 (green), and 120 min (pink). ( $\lambda_{\text{exc}} = 315$  nm).

Sampling was performed for up to 120 min, and the results presented in Figure 6 clearly show that OH<sup>•</sup> was not formed in the case of the silver-based photocatalysts, while it was clearly formed in the case of TiO<sub>2</sub>.

#### 2.4. Photocatalytic Mechanism

The redox potentials of the ground and excited states of the selected dyes are shown in Scheme 1 to illustrate that, in principle, they can be oxidized by the h<sup>+</sup> generated in the VB of the photocatalysts and they can also inject an e<sup>-</sup> in the CBs of the semiconductors upon the absorption of visible light of the appropriate wavelength, since both processes are thermodynamically feasible for all these dyes.



**Scheme 1.** Redox potentials (in V vs. NHE) of the semiconductors and synthetic dyes.

The photodegradation achieved upon the irradiation of the dyes in the presence of TiO<sub>2</sub> could have been the result of Equation (1) (Scheme 2) followed by the generation of hydroxyl radicals (Equation (4)) that were eventually responsible for the oxidation of dyes (Equation (8)). The direct oxidation of dyes by h<sup>+</sup> (VB), as described in Equation (7), would not have competed in this case with the favorable formation of OH<sup>•</sup>, according to the different concentrations of H<sub>2</sub>O and dye molecules on the surface of TiO<sub>2</sub> and the known efficiency of the formation of OH<sup>•</sup> by TiO<sub>2</sub> [57]. In addition, the absorption of light by the dyes followed by the injection of an electron from their excited states into the CB, and the subsequent oxidation (Equations (9)–(11)) could, in principle, have been operating for the azo dyes upon the illumination centered at 420 or 450 nm or in the case of RhB and BB at 450 nm. However, a careful analysis of the results obtained for the case of TZ and OII at the two wavelengths (Figures 4 and 5) and the effect of the addition of scavengers (Figures 6 and 7) suggested the formation of O<sub>2</sub><sup>•-</sup> as a result of Equations (1) and (3) or Equations (9) and (10), together with the formation of OH<sup>•</sup> (Equation (4)), which was eventually more efficient in producing the abatement of the azo dyes and thus explained that they remained stable at 450 nm. The same was true for the abatement of RhB at 420 nm, while the reactivity observed for this dye at 450 nm cannot be explained by direct irradiation of TiO<sub>2</sub>; it could only be explained as a result of the processes described in Equations (9)–(11).

TiO <sub>2</sub> + light (< 400 nm)	→ e <sup>-</sup> (CB) <sub>TiO<sub>2</sub></sub> + h <sup>+</sup> (VB) <sub>TiO<sub>2</sub></sub>	Equation (1)
Ag <sub>3</sub> PO <sub>4</sub> + light (< 535 nm)	→ e <sup>-</sup> (CB) <sub>Ag<sub>3</sub>PO<sub>4</sub></sub> + h <sup>+</sup> (VB) <sub>Ag<sub>3</sub>PO<sub>4</sub></sub>	Equation (2)
e <sup>-</sup> (CB) <sub>TiO<sub>2</sub></sub> + O <sub>2</sub>	→ O <sub>2</sub> <sup>•-</sup>	Equation (3)
h <sup>+</sup> (VB) <sub>TiO<sub>2</sub></sub> + H <sub>2</sub> O	→ OH <sup>•</sup> + H <sup>+</sup>	Equation (4)
2 e <sup>-</sup> (CB) <sub>Ag<sub>3</sub>PO<sub>4</sub></sub> + O <sub>2</sub> + 2 H <sup>+</sup>	→ H <sub>2</sub> O <sub>2</sub>	Equation (5)
H <sub>2</sub> O <sub>2</sub> + e <sup>-</sup>	→ OH <sup>•</sup> + OH <sup>-</sup>	Equation (6)
h <sup>+</sup> (VB) <sub>TiO<sub>2</sub> or Ag<sub>3</sub>PO<sub>4</sub></sub> + Dye	→ Dye <sup>•+</sup>	Equation (7)
OH <sup>•</sup> + Dye	→ Oxidation products	Equation (8)
Dye + light	→ Dye <sup>*</sup>	Equation (9)
Dye <sup>*</sup> + Photocatalyst	→ Dye <sup>•+</sup> + e <sup>-</sup> (CB) <sub>TiO<sub>2</sub> or Ag<sub>3</sub>PO<sub>4</sub></sub>	Equation (10)
Dye <sup>•+</sup> + O <sub>2</sub>	→ Oxidation products	Equation (11)

**Scheme 2.** Potential steps in the degradation of dyes photocatalyzed by TiO<sub>2</sub> or Ag<sub>3</sub>PO<sub>4</sub>.

Similar values for the pseudo-first order rate constants were determined for all dyes upon irradiation at 420 nm in the presence of TiO<sub>2</sub>, thus indicating a similar reactivity. This could be mainly attributed to the generation and subsequent reactivity of the hydroxyl radical. Analogously, upon irradiation at 450 nm, the determined values for the pseudo-first order rate constants for all dyes were in the same order of magnitude except for RhB. Thus, the injection of an electron from the excited state of TZ, OII, and BB into the conduction band of TiO<sub>2</sub> and subsequent reactivity of the generated radical cations constitute a very inefficient degradation pathway.

The observed photodegradation of dyes in the presence of Ag<sub>3</sub>PO<sub>4</sub> can be explained according to Equations (2) or (9) (Scheme 2), followed by either Equation (7) (since no formation of OH<sup>-</sup> was observed; see Figure 8 and Figure S7) or Equations (10) and (11), although the contribution of the processes described in Equations (5) and (6) could not be disregarded (see the effect of IPA in the reactivity in Figures 7 and 8 for OII and BB at 420 nm, and for OII when irradiation was performed at 450 nm). Nevertheless, the main participation of Equation (7) over the other alternatives in all cases could be demonstrated upon careful analyses of the photodegradation achieved in the cases of RhB and BB. These two dyes were efficiently photodegraded in the presence of Ag<sub>3</sub>PO<sub>4</sub> semiconductors at 420 nm, which is a piece of evidence of the oxidative potential of h<sup>+</sup> (VB)<sub>Ag<sub>3</sub>PO<sub>4</sub></sub>. Though the formation

of  $O_2^{\cdot-}$  from the  $e^-$  injected in the  $(VB)_{Ag_3PO_4}$  was not thermodynamically feasible, experiments in the presence of BQ (Figures 7 and 8) pointed to the potential of the excited dyes to directly generate  $O_2^{\cdot-}$ , as has been already described for dissolved organic matter or drugs under irradiation [58–62].

Though the results obtained at the different wavelengths were not comparable, the participation of the process described in Equations (10) and (11) could not be disregarded for RhB and BB when the photodegradations were performed at 450 nm, where both dyes absorbed.

The performance of the hybrid material was comparable to the rest of the silver-based catalysts, pointing to an efficient  $e^-$  transfer from the dyes to the photogenerated holes in the  $VB_{Ag_3PO_4}$ . Nevertheless, the results from the experiments in the presence of scavengers suggested the formation of the less reactive  $O_2^{\cdot-}$ , as well as the marginal generation of hydroxyl radicals.

Overall, the obtained results pointed to a high oxidative potential of  $h^+$   $(VB)_{Ag_3PO_4}$ , comparable to or even higher than that of  $OH^{\cdot}$  (photogenerated only in the case of  $TiO_2$  upon irradiation centered at 420 nm), although a quantitative analysis with different illumination sources was difficult to make. In other words, the photodegradation of dyes at 450 nm in the presence of  $Ag_3PO_4$  materials, even though hydroxyl radicals were not generated, appears as an efficient alternative. In this sense, efforts in trying to increase the stability of  $Ag_3PO_4$  or to investigate of the potential of other semiconductors with the ability to absorb visible light and with high oxidant  $h^+$   $(VB)$ —in addition to other efforts focused on doping—could be alternative options to explore  $TiO_2$  to enlarge its absorption into the visible region.

### 3. Materials and Methods

#### 3.1. Chemicals

Tartrazine, Orange II, rhodamine B, Brilliant Blue FCF,  $AgNO_3$ ,  $CH_3CO_2Ag$ ,  $Na_2HPO_4$ ,  $Na_3PO_4 \cdot 12H_2O$ ,  $TiO_2$  P25 Degussa, 2-propanol, *p*-benzoquinone, ammonium oxalate, terephthalic acid, and  $NH_3$  were from Sigma Aldrich. The water used in all the experiments was Milli-Q grade. All the reagents of this work were of analytical grade and used without further purifications.

#### 3.2. Preparation of the Photocatalysts

Several  $Ag_3PO_4$  photocatalysts were prepared with different morphologies following slight modifications of the protocol developed by Bi et al. [20,63]. Moreover, a hybrid  $Ag_3PO_4$ – $TiO_2$  with a molar ratio 3:10 was synthesized using the procedure described by Yao et al. [48]. More specific typical procedures follow:

For the  $Ag_3PO_4$  rhombic dodecahedrons, 0.8 g of  $CH_3CO_2Ag$  was dissolved in distilled water at 60 °C whilst stirring until a saturated solution was obtained. Then, 32 mL of aqueous  $Na_2HPO_4$  (0.45 M) were added dropwise at 60 °C. Immediately, a yellow precipitate formed. The mixture was stirred in the dark for one hour at 60 °C to ensure that the reaction was complete, after which it was cooled naturally to room temperature. The product was centrifuged at 6000 rpm for 30 min and then cleaned with distilled water before being re-centrifuged. This cleaning process was repeated three times before leaving the  $Ag_3PO_4$  rhombic dodecahedrons in a vacuum desiccator until dry.

For the  $Ag_3PO_4$  cubes, 0.4 g of  $AgNO_3$  was dissolved in distilled water at 60 °C whilst stirring to make a saturated solution. Then, aqueous  $NH_3$  (0.1 M) was added dropwise until the solution turned transparent. Next, 31.4 mL of aqueous  $Na_2HPO_4$  (0.45 M) were added dropwise at 60 °C with continuous stirring until a fine yellow precipitate was formed. The mixture was left to stir for an hour to ensure that the reaction was complete, and then it was cooled naturally to room temperature. The crude was centrifuged at 6000 rpm for 30 min and washed twice with distilled water. The wet  $Ag_3PO_4$  cubes were left in a vacuum desiccator until dry.

For the  $Ag_3PO_4$  spheres, 0.34 g of  $AgNO_3$  was dissolved in distilled water at 60 °C whilst stirring to make a saturated solution. Then, 30 mL of aqueous  $Na_3PO_4$  (0.07 M) were added dropwise at 60 °C whilst continuously stirring until a yellow precipitate was formed. The solution was left to stir for an

hour and then cooled naturally to room temperature. The product was centrifuged at 6000 rpm for 30 min and then cleaned with distilled water before being re-centrifuged. This cleaning process was repeated three times, and the wet  $\text{Ag}_3\text{PO}_4$  spheres were left in a vacuum desiccator until dry.

For the  $\text{Ag}_3\text{PO}_4\text{-TiO}_2$  hybrid heterostructures, in a typical procedure, the heterostructures were prepared by dispersing 0.8 g of commercial  $\text{TiO}_2$  P25 Degussa in 25 mL of distilled water and sonicating for 5 min. Immediately, 1.5 g of  $\text{AgNO}_3$  was added to the aqueous  $\text{TiO}_2$  suspension and stirred for 10 min. Next, 25 mL of aqueous  $\text{Na}_3\text{PO}_4$  (0.13 M) were added dropwise to the reaction mixture until the suspension turned from white to yellow. The mixture was left to stir for 3 h and centrifuged at 6000 rpm for 30 min. The solid was cleaned with distilled water and re-centrifuged. This cleaning process was repeated three times, and the wet  $\text{Ag}_3\text{PO}_4\text{-TiO}_2$  hybrid was left in a vacuum desiccator until dry.

### 3.3. Scanning Electron Microscopy Analysis

A Leica EM MED020 high vacuum coater (Leica, Wetzlar, Germany) was used to deposit a fine layer of gold nanoparticles over the sample to avoid charging and modifying the  $\text{Ag}_3\text{PO}_4$  topography. Pictures were taken with a Zeiss Ultra 55 field emission scanning electron microscope (FESEM) (Zeiss, Oberkochen, Germany), which has a 1.5 nm resolution when working at 3 kV. Samples were ground using a pestle and mortar to ensure as little agglomeration of nanoparticles as possible. These finely ground particles were connected to a sample holder using double-sided conductive tape to avoid charging of the sample by the electron beam. Examination took place in a vacuum. To avoid bias sampling, several images were taken randomly. The average size of particles was determined by measuring the diameter of a minimum of 50 particles from the random images.

### 3.4. Photophysical Experiments

The diffuse reflectance of the  $\text{Ag}_3\text{PO}_4$  photocatalysts and the hybrid  $\text{Ag}_3\text{PO}_4\text{-TiO}_2$  were recorded using a Cary 5000 from Agilent Technologies (Agilent Technologies, Santa Clara, USA) equipped with an integrating sphere. Barium sulphate ( $\text{BaSO}_4$ ) was used as a white standard. Then, the absorption spectra were obtained from the reflectance spectra by means of Kubelka–Munk transformations. A Shimadzu UV-2101PC spectrophotometer (Shimadzu Corporation, Kyoto, Japan) was employed to record the UV/Vis absorption spectra of the food dyes. All the spectra were recorded at room temperature using quartz cells of 1 cm optical path length.

The formation of hydroxyl radicals was evaluated using a Photon Technology International (PTI) LPS-220B spectrometer (Horiba Ltd., Kyoto, Japan). Emissions from solutions were recorded between 350 and 600 nm at different times ( $\lambda_{\text{exc}} = 315$  nm). As a matter of fact, the emissions centered at approximately 426 nm corresponding to 2-hydroxyterephthalic acid acted as evidence for the formation of hydroxyl radicals.

### 3.5. Photocatalytic Degradation of Dyes

Experiments were carried out in parallel to permit direct comparison. Typically, 2.5 mg of photocatalysts were added to 5 mL of an aqueous solution of each dye ( $5 \times 10^{-5}$  M). Pyrex test-tubes were stirred in the dark for 30 min to ensure that the adsorption/desorption equilibrium of dye on photocatalyst had been reached prior to irradiation. Irradiation at 420 nm was performed using a Luzchem photoreactor (model LZC-4 V) (Luzchem Research Inc., Ottawa, Canada) equipped with 8 fluorescent lamps emitting at max = 420 nm, while irradiation at 450 nm was performed using a home-made circular photoreactor made with a spiral set-up of 2.5 m strip green LEDs ( $\lambda_{\text{em}}$  centered at 450 nm), Samsung SMD5630IP20 of 40 W from LEDBOX.

Monitoring the photodegradation of the dyes was based on the absorbance of the aliquots (taken at different times and centrifuged in a Hettich EBA 21 centrifuge) recorded on an Agilent Cary 50 UV-visible spectrophotometer (Agilent Technologies, Santa Clara, USA).

A series of experiments were performed in the presence of IPA ( $1 \times 10^{-1}$  M), BQ ( $1 \times 10^{-4}$  M), and AO ( $1 \times 10^{-4}$  M) as scavengers for  $\text{OH}\cdot$ ,  $\text{O}_2^{\cdot-}$ , and  $\text{h}^+$ , respectively, under the experimental conditions described above.

To evaluate the formation of hydroxyl radicals, individual mixtures of each photocatalyst (0.5 g/L) in aqueous solutions containing NaOH ( $2 \times 10^{-3}$  M) and terephthalic acid ( $5 \times 10^{-4}$  M) were irradiated at 450 nm for the  $\text{Ag}_3\text{PO}_4$ -based photocatalysts and in UV for the  $\text{TiO}_2$ .

#### 4. Conclusions

Silver phosphate photocatalysts have demonstrated that the hydroxyl radical is not the only reactive oxygen species for semiconductor photocatalysts to produce the abatement of synthetic dyes. In fact, the synthesized  $\text{Ag}_3\text{PO}_4$  materials have proven successful, even if they are not to be able to generate hydroxyl radicals. This is mainly due to the oxidative potential of the photogenerated holes in the VB, although the formation of superoxide anion directly from the excited dyes has been evidenced in the presence of scavengers, and the direct electron transfer from the excited dyes to the CB of the photocatalysts cannot be disregarded. By contrast, the performance of  $\text{TiO}_2$  is only comparable at shorter wavelengths due to the generation of hydroxyl radicals; however, it loses efficiency under visible light irradiation since the formed superoxide radical anion is not as efficient as hydroxyl radicals in producing the abatement of dyes. Therefore, visible-light absorbing photocatalysts with an unlikely recombination of electron-hole pairs and an appropriate potential of their CB constitute good alternatives that can be efficiently applied for wastewater remediation.

**Supplementary Materials:** The following are available online at <http://www.mdpi.com/2073-4344/10/7/774/s1>, Figure S1: Normalized absorbance of tartrazine (pink), Orange II (red), rhodamine B (black) and Brilliant Blue FCF (blue); Figure S2: Emission spectrum of Luzchem photoreactor (model LZC-4 V) with 14 bulbs emitting at 420 nm (data kindly provided by Luzchem Research, Inc.); Figure S3: Emission spectrum of homemade photoreactor emitting at 450 nm; Figure S4: Photolysis of TZ (A), OII (B), RhB (C), and BB (D) under 420 nm light; Figure S5: Photolysis of TZ (A), OII (B), RhB (C), and BB (D) under 450 nm LED light; Figure S6: Dark experiments of TZ (A), OII (B), RhB (C), and BB (D) in the presence of  $\text{Ag}_3\text{PO}_4$  cubes (●),  $\text{Ag}_3\text{PO}_4$  rhombic dodecahedrons (▲),  $\text{Ag}_3\text{PO}_4$  spheres (▼), hybrid  $\text{TiO}_2/\text{Ag}_3\text{PO}_4$  (◆), or  $\text{TiO}_2$  (■); Figure S7: Emission spectra of a solution of terephthalic acid (0.5 mM in 2 mM aqueous NaOH) recorded at different irradiation times in the presence of  $\text{Ag}_3\text{PO}_4$  cubes (A),  $\text{Ag}_3\text{PO}_4$  rhombic dodecahedrons (B),  $\text{Ag}_3\text{PO}_4$  spheres (C), hybrid  $\text{Ag}_3\text{PO}_4\text{-TiO}_2$  (D), or  $\text{TiO}_2$  (E), ( $\lambda_{\text{exc}} = 315$  nm); Figure S8: Plot of the ln of the relative concentration of TZ (a); OII (b), RhB (c) and BB (d) vs time in the presence of  $\text{Ag}_3\text{PO}_4$  cubes (●),  $\text{Ag}_3\text{PO}_4$  rhombic (▲),  $\text{Ag}_3\text{PO}_4$  spheres (▼), hybrid  $\text{Ag}_3\text{PO}_4\text{-TiO}_2$  (◆) or  $\text{TiO}_2$  (■), under 420 nm irradiation. Initial concentrations:  $5 \times 10^{-5}$  M (dye) and 0.5 g/L (photocatalyst) in aerated aqueous media; Figure S9: Plot of the ln of the relative concentration of TZ (a); OII (b), RhB (c) and BB (d) vs time in the presence of  $\text{Ag}_3\text{PO}_4$  cubes (●),  $\text{Ag}_3\text{PO}_4$  rhombic (▲),  $\text{Ag}_3\text{PO}_4$  spheres (▼), hybrid  $\text{Ag}_3\text{PO}_4\text{-TiO}_2$  (◆) or  $\text{TiO}_2$  (■), under 450 nm irradiation. Initial concentrations:  $5 \times 10^{-5}$  M (dye) and 0.5 g/L (photocatalyst) in aerated aqueous media.

**Author Contributions:** Conceptualization, M.A.M. and M.L.M.; data curation, A.P.; formal analysis, A.P.; funding acquisition, M.A.M. and M.L.M.; investigation, A.P., A.B., and P.F.J.; methodology, A.P., A.B., and P.F.J.; project administration, M.A.M. and M.L.M.; supervision, M.L.M.; validation, A.P.; writing—original draft, A.P., A.B., and P.F.J.; writing—review and editing, M.A.M. and M.L.M. All authors have read and agreed to the published version of the manuscript.

**Funding:** This research was funded by Spanish Government (Grant SEV-2016-0683), Generalitat Valenciana (Prometeo Program) and H2020/Marie Skłodowska-Curie Actions under the AQUAlity project (Reference: 765860).

**Acknowledgments:** The authors would like to acknowledge H2020/Marie Skłodowska-Curie Actions under the AQUAlity project (Reference: 765860). Conselleria d'Educació, Investigació, Cultura i Esport (PROMETEO/2017/075 and GRISOLÍAP/2017/005) is gratefully acknowledged.

**Conflicts of Interest:** The authors declare no conflict of interest.

#### References

1. Boczkaj, G.; Fernandes, A. Wastewater treatment by means of advanced oxidation processes at basic pH conditions: A review. *Chem. Eng. J.* **2017**, *320*, 608–633. [CrossRef]
2. Miklos, D.B.; Remy, C.; Jekel, M.; Linden, K.G.; Drewes, J.E.; Hubner, U. Evaluation of advanced oxidation processes for water and wastewater treatment—A critical review. *Water Res.* **2018**, *139*, 118–131. [CrossRef] [PubMed]

3. Gagol, M.; Przyjazny, A.; Boczkaj, G. Wastewater treatment by means of advanced oxidation processes based on cavitation-A review. *Chem. Eng. J.* **2018**, *338*, 599–627. [[CrossRef](#)]
4. Rizzo, L. Bioassays as a tool for evaluating advanced oxidation processes in water and wastewater treatment. *Water Res.* **2011**, *45*, 4311–4340. [[CrossRef](#)] [[PubMed](#)]
5. Vaiano, V.; Iervolino, G.; Rizzo, L.; Sannino, D. Advanced Oxidation Processes for the Removal of Food Dyes in Wastewater. *Curr. Org. Chem.* **2017**, *21*, 1068–1073. [[CrossRef](#)]
6. Fernandez, C.; Larrechi, M.S.; Callao, M.P. An analytical overview of processes for removing organic dyes from wastewater effluents. *TrAC Trend Anal. Chem.* **2010**, *29*, 1202–1211. [[CrossRef](#)]
7. Gregory, P. Azo dyes-Structure carcinogenicity relationships. *Dye. Pigment.* **1986**, *7*, 45–56. [[CrossRef](#)]
8. Konstantinou, I.K.; Albanis, T.A. TiO<sub>2</sub>-assisted photocatalytic degradation of azo dyes in aqueous solution: Kinetic and mechanistic investigations: A review. *Appl. Catal. B* **2004**, *49*, 1–14. [[CrossRef](#)]
9. Fujishima, A.; Rao, T.N.; Tryk, D.A. Titanium dioxide photocatalysis. *J. Photochem. Photobiol. C* **2000**, *1*, 1–21. [[CrossRef](#)]
10. Gligorovski, S.; Strekowski, R.; Barbati, S.; Vione, D. Environmental Implications of Hydroxyl Radicals (•OH). *Chem. Rev.* **2015**, *115*, 13051–13092. [[CrossRef](#)]
11. Mills, A.; Le Hunte, S. An overview of semiconductor photocatalysis. *J. Photochem. Photobiol. A* **1997**, *108*, 1–35. [[CrossRef](#)]
12. Han, F.; Kambala, V.S.R.; Srinivasan, M.; Rajarathnam, D.; Naidu, R. Tailored titanium dioxide photocatalysts for the degradation of organic dyes in wastewater treatment: A review. *Appl. Catal. A* **2009**, *359*, 25–40. [[CrossRef](#)]
13. Rauf, M.A.; Meetani, M.A.; Hisaindee, S. An overview on the photocatalytic degradation of azo dyes in the presence of TiO<sub>2</sub> doped with selective transition metals. *Desalination* **2011**, *276*, 13–27. [[CrossRef](#)]
14. Ismael, M. Highly effective ruthenium-doped TiO<sub>2</sub> nanoparticles photocatalyst for visible-light-driven photocatalytic hydrogen production. *New J. Chem.* **2019**, *43*, 9596–9605. [[CrossRef](#)]
15. Ismael, M. Enhanced photocatalytic hydrogen production and degradation of organic pollutants from Fe (III) doped TiO<sub>2</sub> nanoparticles. *J. Environ. Chem. Eng.* **2020**, *8*, 103676. [[CrossRef](#)]
16. Rajeshwar, K.; Osugi, M.E.; Chanmanee, W.; Chenthamarakshan, C.R.; Zaroni, M.V.B.; Kajitvichyanukul, P.; Krishnan-Ayer, R. Heterogeneous photocatalytic treatment of organic dyes in air and aqueous media. *J. Photochem. Photobiol. C* **2008**, *9*, 171–192. [[CrossRef](#)]
17. Ismael, M.; Elhaddad, E.; Taffa, D.H.; Wark, M. Synthesis of Phase Pure Hexagonal YFeO<sub>3</sub> Perovskite as Efficient Visible Light Active Photocatalyst. *Catalysts* **2017**, *7*, 326. [[CrossRef](#)]
18. Ismael, M.; Wark, M. Perovskite-type LaFeO<sub>3</sub>: Photoelectrochemical Properties and Photocatalytic Degradation of Organic Pollutants Under Visible Light Irradiation. *Catalysts* **2019**, *9*, 342. [[CrossRef](#)]
19. Yi, Z.; Ye, J.; Kikugawa, N.; Kako, T.; Ouyang, S.; Stuart-Williams, H.; Withers, R.L. An orthophosphate semiconductor with photooxidation properties under visible-light irradiation. *Nat. Mater.* **2010**, *9*, 559–564. [[CrossRef](#)]
20. Bi, Y.; Ouyang, S.; Umezawa, N.; Cao, J.; Ye, J. Facet Effect of Single-Crystalline Ag<sub>3</sub>PO<sub>4</sub> Sub-microcrystals on Photocatalytic Properties. *J. Am. Chem. Soc.* **2011**, *133*, 6490–6492. [[CrossRef](#)]
21. Jinfeng, Z.; Tao, Z. Preparation and characterization of highly efficient and stable visible-light-responsive photocatalyst AgBr/Ag<sub>3</sub>PO<sub>4</sub>. *J. Nanomater.* **2013**, *2013*, 565074. [[CrossRef](#)]
22. Wardman, P. Reduction potentials of one-electron couples involving free-radicals in aqueous solution. *J. Phys. Chem. Ref. Data* **1989**, *18*, 1637–1755. [[CrossRef](#)]
23. Pitre, S.P.; McTiernan, C.D.; Scaiano, J.C. Understanding the Kinetics and Spectroscopy of Photoredox Catalysis and Transition-Metal-Free Alternatives. *Acc. Chem. Res.* **2016**, *49*, 1320–1330. [[CrossRef](#)]
24. Cao, J.; Luo, B.; Lin, H.; Xu, B.; Chen, S. Visible light photocatalytic activity enhancement and mechanism of AgBr/Ag<sub>3</sub>PO<sub>4</sub> hybrids for degradation of methyl orange. *J. Hazard. Mater.* **2012**, *217–218*, 107–115. [[CrossRef](#)] [[PubMed](#)]
25. Ge, M.; Zhu, N.; Zhao, Y.; Li, J.; Liu, L. Sunlight-Assisted Degradation of Dye Pollutants in Ag<sub>3</sub>PO<sub>4</sub> Suspension. *Ind. Eng. Chem. Res.* **2012**, *51*, 5167–5173. [[CrossRef](#)]
26. Ge, M. Photodegradation of rhodamine B and methyl orange by Ag<sub>3</sub>PO<sub>4</sub> catalyst under visible light irradiation. *Chin. J. Catal.* **2014**, *35*, 1410–1417. [[CrossRef](#)]

27. Qamar, M.; Elsayed, R.B.; Alhooshani, K.R.; Ahmed, M.I.; Bahnemann, D.W. Chemoselective and highly efficient conversion of aromatic alcohols into aldehydes photo-catalyzed by  $\text{Ag}_3\text{PO}_4$  in aqueous suspension under simulated sunlight. *Catal. Commun.* **2015**, *58*, 34–39. [[CrossRef](#)]
28. Taheri, M.E.; Petala, A.; Frontistis, Z.; Mantzavinos, D.; Kondarides, D.I. Fast photocatalytic degradation of bisphenol A by  $\text{Ag}_3\text{PO}_4/\text{TiO}_2$  composites under solar radiation. *Catal. Today* **2017**, *280*, 99–107. [[CrossRef](#)]
29. Li, X.; Xu, P.; Chen, M.; Zeng, G.; Wang, D.; Chen, F.; Tan, X. Application of silver phosphate-based photocatalysts: Barriers and solutions. *Chem. Eng. J.* **2019**, *366*, 339–357. [[CrossRef](#)]
30. Zwara, J.; Grabowska, E.; Klimczuk, T.; Lisowski, W.; Zaleska-Medynska, A. Shape-dependent enhanced photocatalytic effect under visible light of  $\text{Ag}_3\text{PO}_4$  particles. *J. Photochem. Photobiol. A* **2018**, *367*, 240–252. [[CrossRef](#)]
31. Petala, A.; Spyrou, D.; Frontistis, Z.; Mantzavinos, D.; Kondarides, D.I. Immobilized  $\text{Ag}_3\text{PO}_4$  photocatalyst for micro-pollutants removal in a continuous flow annular photoreactor. *Catal. Today* **2019**, *328*, 223–229. [[CrossRef](#)]
32. Cruz-Filho, J.F.; Costa, T.M.S.; Lima, M.S.; Silva, L.J.; Santos, R.S.; Cavalcante, L.S.; Luz, G.E. Effect of different synthesis methods on the morphology, optical behavior, and superior photocatalytic performances of  $\text{Ag}_3\text{PO}_4$  sub-microcrystals using white-light-emitting diodes. *J. Photochem. Photobiol. A* **2019**, *377*, 14–25. [[CrossRef](#)]
33. Zhu, C.; Li, Y.; Yang, Y.; Chen, Y.; Yang, Z.; Wang, P.; Feng, W. Influence of operational parameters on photocatalytic decolorization of a cationic azo dye under visible-light in aqueous  $\text{Ag}_3\text{PO}_4$ . *Inorg. Chem. Commun.* **2020**, *115*, 107850. [[CrossRef](#)]
34. Raza, N.; Raza, W.; Gul, H.; Azam, M.; Lee, J.; Vikrant, K.; Kim, K.-H. Solar-light-active silver phosphate/titanium dioxide/silica heterostructures for photocatalytic removal of organic dye. *J. Clean. Prod.* **2020**, *254*, 120031. [[CrossRef](#)]
35. Tab, A.; Bellal, B.; Belabed, C.; Dahmane, M.; Trari, M. Visible light assisted photocatalytic degradation and mineralization of Rhodamine B in aqueous solution by  $\text{Ag}_3\text{PO}_4$ . *Optik* **2020**, *214*, 164858. [[CrossRef](#)]
36. Hamrouni, A.; Azzouzi, H.; Rayes, A.; Palmisano, L.; Ceccato, R.; Parrino, F. Enhanced Solar Light Photocatalytic Activity of Ag Doped  $\text{TiO}_2\text{-Ag}_3\text{PO}_4$  Composites. *Nanomaterials* **2020**, *10*, 795. [[CrossRef](#)]
37. Rawal, S.B.; Sung, S.D.; Lee, W.I. Novel  $\text{Ag}_3\text{PO}_4/\text{TiO}_2$  composites for efficient decomposition of gaseous 2-propanol under visible-light irradiation. *Catal. Commun.* **2012**, *17*, 131–135. [[CrossRef](#)]
38. Ma, J.; Zou, J.; Li, L.; Yao, C.; Zhang, T.; Li, D. Synthesis and characterization of  $\text{Ag}_3\text{PO}_4$  immobilized in bentonite for the sunlight-driven degradation of Orange II. *Appl. Catal. B* **2013**, *134–135*, 1–6. [[CrossRef](#)]
39. Molla, M.; Tateishi, I.; Furukawa, M.; Katsumata, H.; Suzuki, T.; Knaeco, S. Evaluation of Reaction Mechanism for Photocatalytic Degradation of Dye with Self-Sensitized  $\text{TiO}_2$  under Visible Light Irradiation. *Open J. Inorg. Non-Met. Mater.* **2017**, *7*, 1–7.
40. Trasatti, S. The absolute electrode potential: An explanatory note (Recommendations 1986). *Pure Appl. Chem.* **1986**, *58*, 955. [[CrossRef](#)]
41. Ahmad, I.; Murtaza, S.; Ahmed, S. Electrochemical and photovoltaic study of sunset yellow and tartrazine dyes. *Mon. Chem.* **2015**, *146*, 1631–1640. [[CrossRef](#)]
42. Ghoreishi, S.M.; Behpour, M.; Golestaneh, M. Simultaneous voltammetric determination of Brilliant Blue and Tartrazine in real samples at the surface of a multi-walled carbon nanotube paste electrode. *Anal. Methods* **2011**, *3*, 2842–2847. [[CrossRef](#)]
43. Taniguchi, M.; Lindsey, J.S. Database of Absorption and Fluorescence Spectra of >300 Common Compounds for use in PhotochemCAD. *Photochem. Photobiol.* **2018**, *94*, 290–327. [[CrossRef](#)] [[PubMed](#)]
44. Vinodgopal, K.; Wynkoop, D.E.; Kamat, P.V. Environmental Photochemistry on Semiconductor Surfaces: Photosensitized Degradation of a Textile Azo Dye, Acid Orange 7, on  $\text{TiO}_2$  Particles Using Visible Light. *Environ. Sci. Technol.* **1996**, *30*, 1660–1666. [[CrossRef](#)]
45. Vinodgopal, K.; Kamat, P.V. Photochemistry of textile azo dyes. Spectral characterization of excited state, reduced and oxidized forms of Acid Orange 7. *J. Photochem. Photobiol. A* **1994**, *83*, 141–146. [[CrossRef](#)]
46. Romero, N.A.; Nicewicz, D.A. Organic Photoredox Catalysis. *Chem. Rev.* **2016**, *116*, 10075–10166. [[CrossRef](#)]
47. Chebotarev, A.N.; Bevziuk, K.V.; Snigur, D.V.; Bazel, Y.R. The brilliant blue FCF ion-molecular forms in solutions according to the spectrophotometry data. *Russ. J. Phys. Chem. A* **2017**, *91*, 1907–1912. [[CrossRef](#)]

48. Yao, W.; Zhang, B.; Huang, C.; Ma, C.; Song, X.; Xu, Q. Synthesis and characterization of high efficiency and stable  $\text{Ag}_3\text{PO}_4/\text{TiO}_2$  visible light photocatalyst for the degradation of methylene blue and rhodamine B solutions. *J. Mater. Chem.* **2012**, *22*, 4050–4055. [[CrossRef](#)]
49. Molla, M.A.I.; Tateishi, I.; Furukawa, M.; Katsumata, H.; Suzuki, T.; Kaneco, S. Photocatalytic Decolorization of Dye with Self-Dye-Sensitization under Fluorescent Light Irradiation. *ChemEngineering* **2017**, *1*, 8. [[CrossRef](#)]
50. Baiocchi, C.; Brussino, M.C.; Pramauro, E.; Prevot, A.B.; Palmisano, L.; Marci, G. Characterization of methyl orange and its photocatalytic degradation products by HPLC/UV–VIS diode array and atmospheric pressure ionization quadrupole ion trap mass spectrometry. *Int. J. Mass Spectrom.* **2002**, *214*, 247–256. [[CrossRef](#)]
51. Liu, R.; Hu, P.; Chen, S. Photocatalytic activity of  $\text{Ag}_3\text{PO}_4$  nanoparticle/ $\text{TiO}_2$  nanobelt heterostructures. *Appl. Surf. Sci.* **2012**, *258*, 9805–9809. [[CrossRef](#)]
52. Wang, P.; Li, Y.; Liu, Z.; Chen, J.; Wu, Y.; Guo, M.; Na, P. In-situ deposition of  $\text{Ag}_3\text{PO}_4$  on  $\text{TiO}_2$  nanosheets dominated by (001) facets for enhanced photocatalytic activities and recyclability. *Ceram. Int.* **2017**, *43*, 11588–11595. [[CrossRef](#)]
53. Kim, W.J.; Pradhan, D.; Min, B.-K.; Sohn, Y. Adsorption/photocatalytic activity and fundamental natures of  $\text{BiOCl}$  and  $\text{BiOCl}_{1-x}$  prepared in water and ethylene glycol environments, and Ag and Au-doping effects. *Appl. Catal. B* **2014**, *147*, 711–725. [[CrossRef](#)]
54. Cao, J.; Luo, B.; Lin, H.; Chen, S. Synthesis, characterization and photocatalytic activity of  $\text{AgBr}/\text{H}_2\text{WO}_4$  composite photocatalyst. *J. Mol. Catal. A Chem.* **2011**, *344*, 138–144. [[CrossRef](#)]
55. Ishibashi, K.-i.; Fujishima, A.; Watanabe, T.; Hashimoto, K. Detection of active oxidative species in  $\text{TiO}_2$  photocatalysis using the fluorescence technique. *Electrochem. Commun.* **2000**, *2*, 207–210. [[CrossRef](#)]
56. Xiao, Q.; Si, Z.; Zhang, J.; Xiao, C.; Tan, X. Photoinduced hydroxyl radical and photocatalytic activity of samarium-doped  $\text{TiO}_2$  nanocrystalline. *J. Hazard. Mat.* **2008**, *150*, 62–67. [[CrossRef](#)]
57. Hoffmann, M.R.; Martin, S.T.; Choi, W.Y.; Bahnemann, D.W. Environmental Applications of Semiconductor Photocatalysis. *Chem. Rev.* **1995**, *95*, 69–96. [[CrossRef](#)]
58. Reszka, K.; Chignell, C.F. Spectroscopic studies of cutaneous photosensitizing agents IV. The photolysis of benoxaprofen, an anti-inflammatory drug with phototoxic properties. *Photochem. Photobiol.* **1983**, *38*, 281–291. [[CrossRef](#)]
59. Burns, J.M. Methods for reactive oxygen species (ROS) detection in aqueous environments. *Aquat. Sci.* **2012**, *74*, 683–734. [[CrossRef](#)]
60. Zhang, D.; Yan, S.; Song, W. Photochemically Induced Formation of Reactive Oxygen Species (ROS) from Effluent Organic Matter. *Environ. Sci. Technol.* **2014**, *48*, 12645–12653. [[CrossRef](#)]
61. Hayyan, M.; Hashim, M.A.; AlNashef, I.M. Superoxide Ion: Generation and Chemical Implications. *Chem. Rev.* **2016**, *116*, 3029–3085. [[CrossRef](#)] [[PubMed](#)]
62. D, N.; Kondamareddy, K.K.; Bin, H.; Lu, D.; Kumar, P.; Dwivedi, R.K.; Fu, D. Enhanced visible light photodegradation activity of RhB/MB from aqueous solution using nanosized novel Fe–Cd co-modified  $\text{ZnO}$ . *Sci. Rep.* **2018**, *8*, 10691. [[CrossRef](#)] [[PubMed](#)]
63. Bi, Y.; Ouyang, S.; Cao, J.; Ye, J. Facile synthesis of rhombic dodecahedral  $\text{AgX}/\text{Ag}_3\text{PO}_4$  ( $\text{X} = \text{Cl}, \text{Br}, \text{I}$ ) heterocrystals with enhanced photocatalytic properties and stabilities. *Phys. Chem. Chem. Phys.* **2011**, *13*, 10071–10075. [[CrossRef](#)] [[PubMed](#)]

